

UC Berkeley

UC Berkeley Previously Published Works

Title

Distribution of brain iron accrual in adolescence: Evidence from cross-sectional and longitudinal analysis

Permalink

<https://escholarship.org/uc/item/1w169055>

Journal

Human Brain Mapping, 40(5)

ISSN

1065-9471

Authors

Peterson, Eric T
Kwon, Dongjin
Luna, Beatriz
et al.

Publication Date

2019-04-01


DOI

10.1002/hbm.24461

Peer reviewed

RESEARCH ARTICLE

Distribution of brain iron accrual in adolescence: Evidence from cross-sectional and longitudinal analysis

Eric T. Peterson¹ | Dongjin Kwon^{1,2} | Beatriz Luna^{3,4,5} | Bart Larsen^{3,4} | Devin Prouty¹ | Michael D. De Bellis^{6,7} | James Voyvodic⁷ | Chunlei Liu^{7,8,9} | Wei Li⁷ | Kilian M. Pohl¹ | Edith V. Sullivan²  | Adolf Pfefferbaum¹

¹Neuroscience Program, SRI International, Menlo Park, California

²Psychiatry & Behavioral Sciences, Stanford University, Stanford, California

³Psychology, University of Pittsburgh, Pittsburgh, Pennsylvania

⁴Center for the Neural Basis of Cognition, Pittsburgh, Pennsylvania

⁵Western Psychiatric Institute and Clinic, University of Pittsburgh Medical Center, Pittsburgh, Pennsylvania

⁶Healthy Childhood Brain Development Research Program, Psychiatry & Behavioral Sciences, Duke University, Durham, North Carolina

⁷Brain Imaging & Analyses Center, Duke University, Durham, North Carolina

⁸Department of Electrical Engineering and Computer Sciences, University of California, Berkeley, California

⁹Helen Wills Neuroscience Institute, University of California, Berkeley, California

Correspondence

Edith V. Sullivan, Department of Psychiatry and Behavioral Sciences, Stanford University School of Medicine, 401 Quarry Road Stanford, CA 94305.

Email: edie@stanford.edu

Funding information

Moldow Women's Hope and Healing Fund; National Institute on Alcohol Abuse and Alcoholism, Grant/Award Number:

AA021681AA021690AA021691AA0216

92AA021695AA021696AA021697K05

AA017168; National Institutes of Health,

Grant/Award Numbers: AA017168, K05,

AA021691, AA021690, AA021681,

AA021696, AA021692, AA021695,

AA021697

Abstract

To track iron accumulation and location in the brain across adolescence, we repurposed diffusion tensor imaging (DTI) and functional magnetic resonance imaging (fMRI) data acquired in 513 adolescents and validated iron estimates with quantitative susceptibility mapping (QSM) in 104 of these subjects. DTI and fMRI data were acquired longitudinally over 1 year in 245 male and 268 female, no-to-low alcohol-consuming adolescents (12–21 years at baseline) from the National Consortium on Alcohol and NeuroDevelopment in Adolescence (NCANDA) study. Brain region average signal values were calculated for susceptibility to nonheme iron deposition: pallidum, putamen, dentate nucleus, red nucleus, and substantia nigra. To estimate nonheme iron, the corpus callosum signal (robust to iron effects) was divided by regional signals to generate estimated R_2 (edw R_2 for DTI) and R_2^* (e R_2^* for fMRI). Longitudinal iron deposition was measured using the normalized signal change across time for each subject. Validation using baseline QSM, derived from susceptibility-weighted imaging, was performed on 46 male and 58 female participants. Normalized iron deposition estimates from DTI and fMRI correlated with age in most regions; both estimates indicated less iron in boys than girls. QSM results correlated highly with DTI and fMRI results (adjusted $R^2 = 0.643$ for DTI, 0.578 for fMRI). Cross-sectional and longitudinal analyses indicated an initial rapid increase in iron, notably in the putamen and red nucleus, that slowed with age. DTI and fMRI data can be repurposed for identifying regional brain iron deposition in developing adolescents as validated with high correspondence with QSM.

KEYWORDS

adolescent, DTI, fMRI, iron, MRI, QSM, susceptibility, SWI

1 | INTRODUCTION

Both healthy, normal aging (Hallgren & Sourander, 1958) and Alzheimer's disease (Hallgren & Sourander, 1960) are associated with

deposition of nonheme iron in selective brain regions (Ropele & Langkammer, 2016). This association has been studied with even greater interest since magnetic resonance imaging (MRI) was shown to detect iron noninvasively in vivo, generating investigations in the amount,

location, and functional relevance of nonheme iron in brain tissue (Bartzokis et al., 1994; Drayer et al., 1986; Vymazal et al., 1995; Vymazal et al., 1999). These studies have generally focused on the deep gray matter structures identified in postmortem studies (Hallgren & Sourander, 1958) where the iron deposition is the highest, increases during normal aging (Bartzokis et al., 1994; Daugherty & Raz, 2016; Haacke et al., 2005; Pfefferbaum, Adalsteinsson, Rohlfing, & Sullivan, 2010), and is even greater in age-related disorders, notably Alzheimer's disease, indicating excess iron accumulation as a biomarker of disease (Daugherty & Raz, 2015; Daugherty & Raz, 2016; Dhenain, Michot, Volk, Picq, & Boller, 1997; Drayer et al., 1986; Fukunaga et al., 2010; Glasser et al., 2016; Glasser & Van Essen, 2011; Haacke et al., 2005; Hallgren & Sourander, 1960; Langkammer et al., 2010; Schenck & Zimmerman, 2004; Walsh & Han, 2014; Ward, Zucca, Duyn, Crichton, & Zecca, 2014). MRI-identified excessive iron accumulation has also been linked with hypertension (Rodrigue, Haacke, & Raz, 2011), obesity (Kullmann et al., 2016), and insulin resistance (Blasco et al., 2014).

Studies of neonates, infants, and young children have established that nutrients from iron are essential for normal development of cortical and fiber tract myelination and associated cognitive and motor functions (review Deoni, Dean III, Joelson, O'Regan, & Schneider, 2018; Stiles & Jernigan, 2010). To the extent that in vivo neuroimaging with susceptibility-weighted imaging (SWI), field-dependent relaxation-rate increase (FDRI), and other methods are able to detect regional nonheme iron, which is a reflection of the nutrient (Bartzokis et al., 2007; Beard & Connor, 2003), neuroimaging offers a method for tracking the iron signal in the adolescent brain, which normally continues development of cortical (Glasser & Van Essen, 2011) and white matter tract (Lebel, Walker, Leemans, Phillips, & Beaulieu, 2008) myelin, presumably requiring iron, and cognition (Casey, Jones, & Hare, 2008).

Pre-MRI iron deposition work was limited to histology (Hallgren & Sourander, 1958). MRI relaxation rates were discovered to be sensitive to iron concentration. Initial MRI investigations used direct measures of relaxivity (i.e., R_2 and R_2^*) as primary indicators of iron (Dhenain et al., 1997; Drayer et al., 1986) and were verified with histology (Haacke et al., 2005; Langkammer et al., 2010). More recent work has focused on semiquantitative and quantitative methods including SWI (Haacke et al., 2005), FDRI (Bartzokis et al., 1994; Pfefferbaum, Adalsteinsson, Rohlfing, & Sullivan, 2009). Quantitative susceptibility mapping (QSM) (Poynton et al., 2015), and R_2' mapping (Gelman et al., 1999; Haacke et al., 2005).

The present study investigated the ability of standard Diffusion Tensor Imaging (DTI) (Pfefferbaum et al., 2010) and functional MRI (fMRI) (Larsen & Luna, 2015) to track the course of nonheme iron (ferritin) (Fukunaga et al., 2010; Haacke et al., 2005) deposition in brain structures that have previously been shown to be susceptible to iron deposition with age (Drayer et al., 1986; Hallgren & Sourander, 1958) in adolescents and young adults. Although several studies have examined iron presence in the brains of adolescents and have shown greater iron signal in subcortical and cerebellar structures known to have high iron content (Larsen & Luna, 2015; Zhang et al., 2018), the samples of teenagers have been small and cross sectional. By contrast, the present study included 513 highly screened adolescents, 384 of

whom were examined a second time 1 year later. The data were collected across five sites participating in the National Consortium on Alcohol and NeuroDevelopment in Adolescence (NCANDA) study (Brown et al., 2015) that necessitated data harmonization as a goal of the analysis. Because DTI and fMRI images are part of most standard acquisition protocols for clinical and research purposes, demonstration of their utility in calculating an estimate of brain iron deposition would allow for repurposing of data for evaluation of brain iron from existing data sets. The metrics from the DTI and fMRI scans were compared against a subset of subjects with SWI data analyzed with QSM as a clinical standard to validate that the effects obtained with DTI and fMRI data reflect nonheme iron.

2 | METHODS

2.1 | Participants

Subjects included 513 no/low alcohol-consuming adolescents and young adults age 12–21 years (15.71 ± 2.33) at the first visit, recruited by the NCANDA study (Brown et al., 2015). Data acquisition was conducted with full IRB approval at the five NCANDA sites across the United States: University of Pittsburgh Medical Center (UPMC), SRI International (SRI), Duke University (Duke), Oregon Health & Science University (OHSU), and University of California San Diego (UCSD). NCANDA is a longitudinal, prospective study of healthy 12–21 year olds (deemed healthy by thorough examination) (Brown et al., 2015) aimed at investigating whether and how the normal neurodevelopmental trajectories of the brain and its many regions and tissue types are diverted with the initiation of appreciable drinking. The drinking threshold was based on National Institute on Alcohol Abuse and Alcoholism guidelines for risky drinking that varied by age and sex. As stated previously (Pfefferbaum et al., 2018), the maximum drinking days was five for those 12–15.9 years old, 11 for those 16–16.9 years old, 23 for those 17–17.9 years old, and 51 for those age 18 and older. The maximum allowable drinks per occasion was three for female participants at any age but varied by age for male participants, for whom the maximum drinks per occasion was three for those 12–13.9 years old, four for those 14–19.9 years old, and five for those age 20 and older.

Of the 513 youth analyzed at baseline, data for 385 were available for the longitudinal analysis; this subgroup was 12–21 years old (mean \pm SD = 15.92 ± 2.36) at baseline and 13–22 years old (16.94 ± 2.36) at the 1-year follow-up. This data set is available through the Scalable Informatics for Biomedical Imaging Studies (Müller-Oehring et al., 2018; Nichols, 2015; Pfefferbaum et al., 2016; Pohl et al., 2016; Rohlfing, Cummins, Henthorn, Chu, & Nichols, 2014) (www.sibis.org) as NCANDA_PUBLIC_1Y_REDCAP_V02, NCANDA_PUBLIC_1Y_STRUCTURAL_V01, NCANDA_PUBLIC_1Y_DIFFUSION_V01, NCANDA_PUBLIC_1Y_RESTINGSTATE_V01.

In addition, 104 subjects, age 12–19 years (15.0 ± 1.75) from the Duke site were scanned at baseline using a multiecho susceptibility and R_2^* mapping scan (Li et al., 2014; Liu, Lee, et al., 2015) specifically to evaluate iron deposition. These data were used to validate the DTI and fMRI scan results on the multisite cohort.

Demographic data (Table 1) were collected through interviews and tests. Data relevant to this analysis comprised age, handedness, body mass index (BMI) percentage, sex, ethnicity (Brown et al., 2015), and working memory speed using the computerized WebCNP battery (Gur et al., 2010) with data taken from Sullivan et al. (2016). All minor participants and at least one parent or participants who were 21 years old at study entry were thoroughly screened for maternal exposure to toxins during pregnancy and for other toxins, drugs, and alcohol thereafter (Brown et al., 2015).

2.2 | MRI acquisition

The multisite protocol was designed to acquire comparable T₁ (IR-SPGR, MPRAGE), DTI, and fMRI data at all five NCANDA sites (Table 2). All collection sites used the same protocol and 3T systems: three sites used GE MR750 and two used Siemens TIM-Trio scanners. All subjects had the same set of MRI scans at each time point used for the analysis.

The Duke site also acquired susceptibility-weighted images based on multiecho SPGR acquisition using a GE MR750 scanner (Table 1).

2.3 | Preprocessing

All DTI and fMRI scans were eddycurrent and EPI-distortion corrected (fMRI with field maps and FSL FUGUE [FMRIB's Utility for Geometrically Unwarping EPIs] and DTI with FSL topup and eddy) (Andersson & Skare, 2002; Jenkinson & Smith, 2001; Smith et al., 2004). The first nondiffusion weighted volume of the DTI and the first fMRI volume were nonrigidly registered to the T₁ structural image via ANTS (Avants, Epstein, Grossman, & Gee, 2008). ANTS was also used to rigidly register all functional images to the first one and then compute average of the fMRI across time. The process was repeated for the DTI $b = 1,000 \text{ s/mm}^2$ sequence by first rigidly aligning the MRIs of all directions to the first nondiffusion weighted volume and then computing the average of DTI across all directions. This completed the DTI and fMRI specific processing. Structural T₁ specific processing was confined to nonrigidly registering the MRI to the SRI24 (Rohlfing, Zahr, Sullivan, & Pfefferbaum, 2010) and cerebellar brain atlases (Diedrichsen, 2006) via ANTS.

To approximate the estimated diffusion-weighted R₂ (or edwR₂) from the DTI sequence, T₂ was estimated by computing the average across all gradient directions. Next, the mean of the resulting average map with respect to the posterior corpus callosum (Drayer et al., 1986) was recoded. The posterior corpus callosum was defined as the corpus callosum on the SRI24 atlas (Rohlfing et al., 2010) posterior to the anterior point of the pallidum. Finally, the average map was divided by that mean value and inverted to determine edwR₂ (i.e., 1/[normalized T₂]). The process was repeated with respect to the average of the resting-state (rs)-fMRI sequence across time to compute T₂^{*}, the normalized T₂^{*}, and the rs-fMRI estimate R₂^{*} (i.e., 1/[normalized T₂^{*}]), which we refer to as eR₂^{*}. Regional and voxel-wise processing, including age regression, was performed using Python 2.7 (Van Rossum, 1991) with the regions defined according to the SRI24 atlas.

The QSM was generated from the susceptibility-weighted images using the in-house software STI Suite (Li et al., 2014; Li, Wu, & Liu,

TABLE 1 Demographics of the participants. The Duke site has the subset of subjects scanned with QSM in parenthesis

| | Site | | | | | | | | | |
|---------------|-------------|-------------|-------------|-------------|-------------|--------------|--------------|-------------|--------------|-------------|
| | UPMC | | SRI | | Duke | | OHSU | | UCSD | |
| | Male | Female | Male | Female | Male | Female | Male | Female | Male | Female |
| Visit 0 (QSM) | | | | | | | | | | |
| N | 25 | 38 | 41 | 62 | 49 | 43 | 46 | 44 | 66 | 57 |
| Age (years) | 16.3 ± 2.53 | 16.2 ± 2.46 | 15.1 ± 1.89 | 15.4 ± 2.13 | 15.2 ± 1.52 | 15.08 ± 1.47 | 14.95 ± 1.96 | 15.1 ± 2.00 | 14.95 ± 1.96 | 15.9 ± 2.75 |
| Ethnicity | 0, 0% | 2, 5% | 9, 17% | 8, 19% | 4, 8% | 4, 9% | 3, 5% | 7, 14% | 7, 13% | 7, 11% |
| Asian | 0, 0% | 2, 5% | 9, 17% | 8, 19% | 4, 8% | 4, 9% | 3, 5% | 7, 14% | 7, 13% | 7, 11% |
| Black | 4, 16% | 10, 24% | 1, 2% | 0, 0% | 16, 33% | 15, 33% | 29, 44% | 23, 40% | 1, 2% | 2, 4% |
| White | 21, 84% | 29, 71% | 41, 77% | 33, 79% | 29, 59% | 27, 59% | 33, 50% | 31, 53% | 41, 80% | 42, 79% |
| Mixed | 0, 0% | 0, 0% | 2, 4% | 1, 2% | 0, 0% | 0, 0% | 1, 2% | 1, 2% | 2, 4% | 2, 3% |
| Visit 1 | | | | | | | | | | |
| N | 20 | 42 | 28 | 58 | 34 | 53 | 31 | 39 | 39 | 46 |
| Age (years) | 17.4 ± 2.52 | 18.1 ± 2.27 | 16.5 ± 1.87 | 16.1 ± 2.24 | 16.1 ± 1.39 | 16.1 ± 2.01 | 17.2 ± 2.63 | 17.6 ± 2.75 | 17.6 ± 2.36 | 16.8 ± 2.41 |
| Ethnicity | 0, 0% | 2, 7% | 7, 21% | 6, 20% | 2, 6% | 1, 2% | 4, 10% | 5, 11% | 6, 11% | 7, 12% |
| Asian | 0, 0% | 2, 7% | 7, 21% | 6, 20% | 2, 6% | 1, 2% | 4, 10% | 5, 11% | 6, 11% | 7, 12% |
| Black | 3, 15% | 6, 21% | 0, 0% | 1, 3% | 11, 35% | 22, 46% | 1, 3% | 2, 4% | 1, 2% | 8, 14% |
| White | 17, 85% | 20, 71% | 26, 76% | 23, 77% | 18, 58% | 24, 50% | 33, 85% | 37, 82% | 47, 87% | 41, 73% |
| Mixed | 0, 0% | 0, 0% | 1, 3% | 1, 3% | 0, 0% | 1, 2% | 1, 3% | 1, 2% | 0, 0% | 0, 0% |

OHSU = Oregon Health & Science University; QSM = quantitative susceptibility mapping; UCSD = University of California San Diego; UPMC = University of Pittsburgh Medical Center; SRI = SRI International.

TABLE 2 Acquisition parameters for the relevant NCANDA scans. Fields not applicable are labeled "N/A"

| Type | DTI | fMRI | Structural (T ₁) | QSM |
|---------------------------------------|-------------------------------------|---------------------|---|--|
| Acquisition method | Spin echo EPI | Gradient echo EPI | Inversion recovery prepared gradient echo | Spoiled gradient echo |
| TE (ms) | 61.1 | 30 | Minimum | 10 echoes: 4.00, 6.82, 9.64, 12.46, 15.28, 18.10, 20.92, 23.74, 26.56, 29.38 |
| TR (ms) | 8,000 | 2,200 | 6 | 41 |
| Flip angle (°) | 90–180 | 79 | 11 | 10 |
| Matrix | 128 × 128 × 64 slices | 64 × 64 × 32 slices | 256 × 256 × 150 | 254 × 288 × 54 slices |
| Voxel size (mm) | 1.875 × 1.875 × .5 | 3.75 × 3.75 × 5 | 0.9375 × 0.9375 × 1.2 | 0.76 × 0.76 × 2 |
| SENSE/ASSET acceleration | 2 | N/A | N/A | N/A |
| Nondiffusion/diffusion volumes | 2/60 | N/A | N/A | N/A |
| Diffusion values (s/mm ²) | 0, 1,000 | N/A | N/A | N/A |
| Derived data | eR ₂ , edwR ₂ | eR ₂ * | N/A | Susceptibility |

DTI = diffusion tensor imaging; EPI = echo-planar imaging; fMRI = functional magnetic resonance imaging; NCANDA = National Consortium on Alcohol and NeuroDevelopment in Adolescence; QSM = quantitative susceptibility mapping.

2011; Liu, Li, et al., 2015). Greater QSM values indicated greater iron presence. QSM data were nonrigidly registered to SRI24 atlas by aligning the last echo of the magnitude data (TE = 29.38) with the T₁-weighted MRI of the atlas using ANTS (Avants et al., 2008). Regional QSM values were defined according to the SRI24 atlas.

2.4 | Statistical analysis

Inclusion criteria for analysis required that all data fields were available and adolescents met criteria for no/low alcohol and drug consumption. The regions of interest (ROIs) analyzed were the left and right pallidum, putamen, cerebellar dentate nucleus, red nucleus, and substantia nigra. Separate regional regression analyses using normalized signal values were performed on the edwR₂ and eR₂* data. Dependent variables considered were the edwR₂ and eR₂* signal; independent variables were age and age squared; and covariate variables were handedness, BMI percentage, supratentorial brain volume, scanning site, sex, ethnicity, and working memory speed. Covariate variables were typically analyzed as independent variables, but covariate correction was performed for most plots by fitting a linear model to the data with the above variables and removing the predicted effects of the covariate variables while leaving the effects of the independent variables. AIC analysis (Venables & Ripley, 2002) was used to remove insignificant covariates for all analyses.

The regional information from the quantitative scans was generated using the same method. The resulting regional average susceptibility values were added to the edwR₂, eR₂*, and demographic variables to create a subset of data from the standard DTI, fMRI, and QSM images.

2.5 | Baseline data analysis

Only the baseline (first) time point data were used in this cross-sectional analysis. For plotting all covariate variables were removed. The best-fit was chosen from either age or age and age squared if the addition of the age-squared variable was significant based on the AIC (Venables & Ripley, 2002).

2.6 | QSM data analysis

The QSM data analysis largely paralleled the data analysis for the DTI and fMRI data. The susceptibility data were all analyzed separately using linear regression with the same dependent and independent variables as used in the baseline data analysis. The susceptibility data were also compared with the edwR₂ and eR₂* metrics using linear regression to establish correspondence.

2.7 | Longitudinal data analysis

Longitudinal iron deposition with age was measured using the normalized signal change across time for each subject. The longitudinal data were fit with linear mixed-effects models (lmer in R) with linear and quadratic models (age and age + age squared). The two models were then tested for superiority with ANOVA. Consistency of the measures between the two scanning sessions was tested with Pearson correlations and intraclass correlations.

3 | RESULTS

3.1 | Normalizing values over imaging modalities

The posterior corpus callosum was used for internal normalization because, while age is a significant factor for both edwR₂ (adjusted $R = 0.101$, $p = .0045$) and eR₂* (adjusted $R = -0.118$, $p = .0010$), the corpus callosum is largely unaffected by iron deposition (Bartzokis et al., 2007) (Figure 1).

3.2 | Site, hemisphere, and ROI effects in relation to age

We conducted three omnibus ANOVAS—one for each iron metric approach—and included age, ROI, hemisphere, and site as factors for the DTI and fMRI metrics and age, ROI, and hemisphere for the QSM analysis (because it was acquired at only one site). In addition to the main effects of the principal factors, interactions involving age were relevant to the current analysis. The ANOVA results, summarized below,

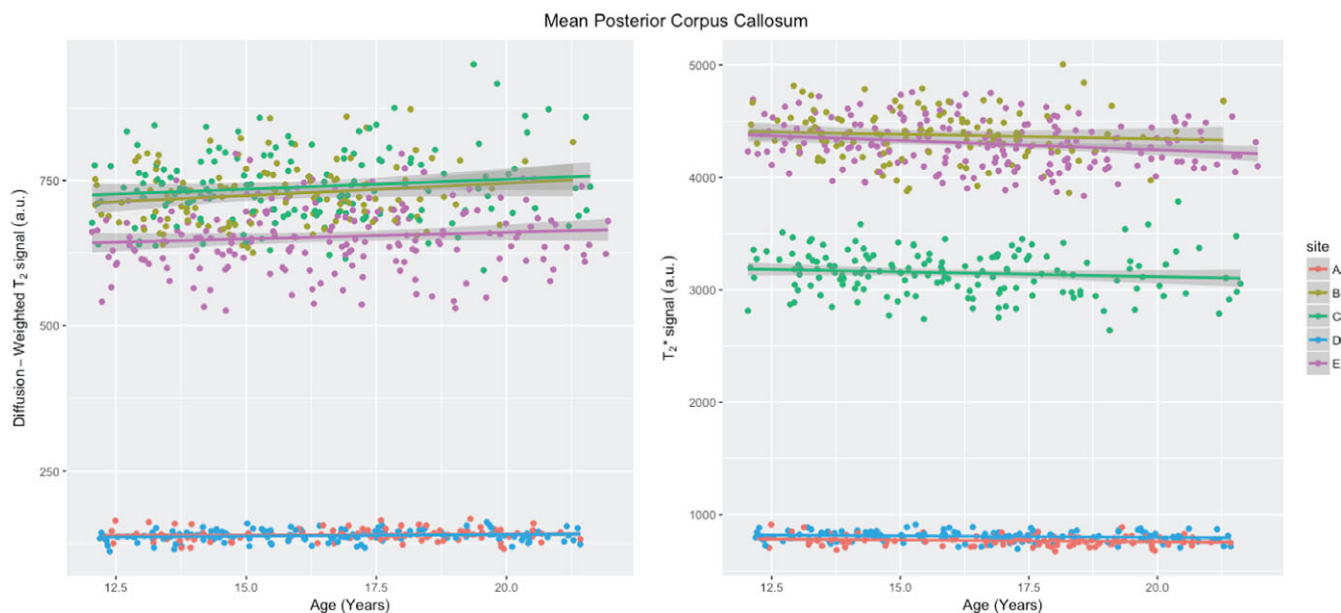


FIGURE 1 Average posterior corpus callosum intensity (normalization value) of diffusion-weighted T_2 ($b = 1,000 \text{ s/mm}^2$) (left) and T_2^* (right) weighted images displayed by imaging site (A–E). This value from the normalization region was used to normalize the images [Color figure can be viewed at wileyonlinelibrary.com]

revealed virtually the same pattern of main effects and interactions for each type of iron estimate.

3.2.1 | DTI iron estimates (edwR_2)

An omnibus ANOVA with four variables (age \times ROI \times hemisphere \times site) yielded four main effects. Specifically, higher iron estimates occurred with older age [$F(df = 15,030) = 1,836.824, p < 2e-16$]. Furthermore, iron estimates varied by ROI [$F(df = 45,030) = 4,760.568, p < 2e-16$], hemisphere such that the iron estimates in the right hemisphere were approximately 3% lower than in the left hemisphere [$F(df = 15,030) = 161.555, p < 2e-16$], and site where Siemens sites had smaller values than GE sites [$F(df = 4,5030) = 357.963, p < 2e-16$]. The only significant interaction involving age was with ROI, indicating that some ROIs showed greater age-related differences than others [$F(df = 45,030) = 65.207, p < 2e-16$]. The three- and four-way interactions involving age were not significant. Thus, the analyses described in Section 2.4 collapsed across site and age and age-squared functions tested for cross-sectional differences in iron estimates across adolescence; the longitudinal analyses also collapsed across hemisphere.

3.2.2 | T_2^* iron estimates (eR_2^*)

An omnibus ANOVA with four variables (age \times ROI \times hemisphere \times site) yielded three main effects. Higher iron estimates occurred with older age [$F(df = 15,025) = 524.859, p < 2e-16$]; iron estimates varied by ROI [$F(df = 45,025) = 2,402.843, p < 2e-16$]; Siemens sites had smaller values than GE sites [$F(df = 45,025) = 55.085, p < 2e-16$]. The only robustly significant interaction involving age was with ROI, indicating that some ROIs showed greater age-related differences than others [$F(df = 45,025) = 24.671, p < 2e-16$]. The three- and four-way interactions involving age were not significant. Apart from one modest interaction (age, ROI, and site [$F(df = 165,025) = 1.720, p = .03645$]), the three- and four-way interactions involving age were not

significant. Thus, further analyses collapsed across site and the longitudinal analyses also collapsed across hemisphere.

3.2.3 | QSM iron estimates

An omnibus ANOVA with three variables (age \times ROI \times hemisphere) yielded two main effects. Higher iron estimates occurred with older age [$F(df = 11,020) = 92.505, p < 2e-16$], and iron estimates varied by ROI [$F(df = 41,020) = 968.940, p < 2e-16$]; iron estimates did not differ between hemispheres [$F(df = 15,025) = 2.003, p < .15701$]. Neither three-way interaction involving age was significant. Thus, the longitudinal analyses also collapsed across hemisphere.

3.3 | Relations between iron metrics, age, demographic, and neuropsychological measures

Voxel-wise normalized signal regressions showed significant correlations with age for the evaluated ROIs and higher than those visually obvious in other brain regions (Figure 2). Regression analysis predicting the edwR_2 and eR_2^* values revealed highly significant effects of age and site on both edwR_2 (Table 3) and edwR_2^* (Table 4) in all ROIs. The edwR_2 (Figure 3) and eR_2^* (Figure 4) signal in all ROIs significantly increased with age. When including age squared, which was significant in most ROIs, the signal showed deceleration with older age, indicating a slowing of iron deposition throughout development.

Age squared was correlated with edwR_2 in all ROIs except for left dentate nucleus. Collection site was highly significant in most cases, and all other factors with edwR_2 were significant in select regions. Specifically, higher BMI was correlated with lower iron signal in the left pallidum and putamen but with greater iron signal in the bilateral dentate nucleus. Faster speed on working memory correlated with lower iron signal in the left dentate nucleus and substantia nigra. Male participants had lower iron levels than female participants in all regions except for the left dentate nucleus. These results are listed in

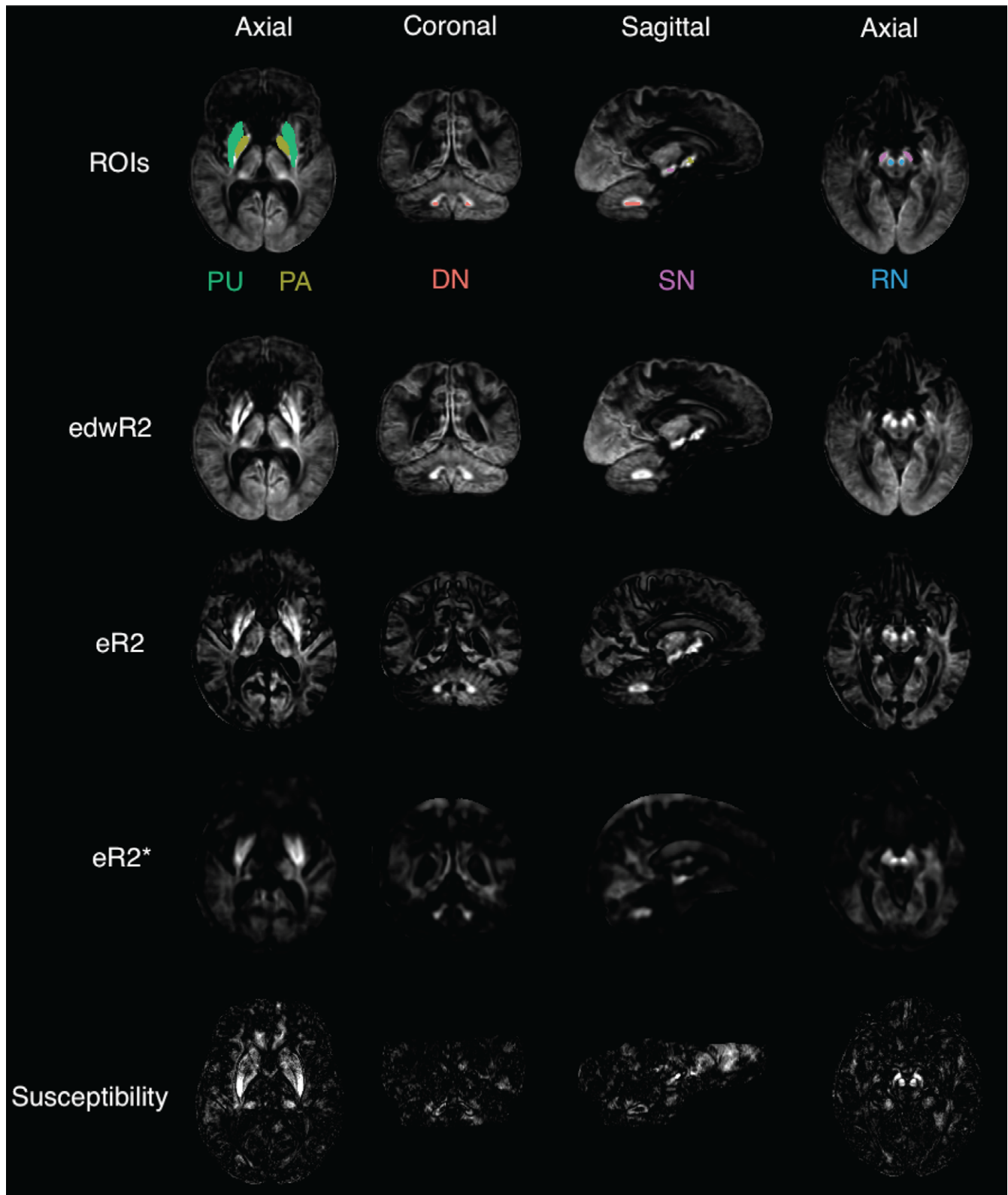


FIGURE 2 r -squared values of all image types linearly regressed with age scaled from 0 to 0.25. The slices are positioned so that all ROIs are visible as the higher r -squared regions. The regions are color coded and the acronyms are as follows: DN = cerebellar dentate nucleus; PA = pallidum; PU = putamen; RN = red nucleus; SN = substantia nigra [Color figure can be viewed at wileyonlinelibrary.com]

Table 3 and the covariate-corrected age-signal plots are shown in Figure 3. The same analysis was performed on the nondiffusion-weighted images and, while the same contrasts were significant, they were not as strong as the diffusion-weighted images $edwR_2$ and are therefore not reported.

For eR_2^* , the age-squared regressions indicated smaller cross-sectional estimates in the latter adolescent years in the bilateral pallidum and substantia nigra. Collection site was again highly significant in most cases. All other factors with eR_2^* were significant in select regions and generally less so than $edwR_2$. Greater BMI correlated with

TABLE 3 Significance matrix showing the t-value (top value in a cell) and p-value (bottom value in a cell) for each variable and region for the edwR₂ data. Note that the site and intercept variables are not shown and positive t-values indicate an increase with edwR₂ and a negative t-value indicates a decrease. N/A values are those which were removed by the AIC procedure

| Region | Age | Age squared | BMI percentile | Race | | | Sex male | Working memory speed z-score |
|------------------------|-------------------------|---------------|----------------|---------------|----------------|------------|---------------|------------------------------|
| | | | | Race black | Race caucasian | Race other | | |
| Dentate nucleus right | t = 4.01 p = 6.5e-05 | -2.63 8.6e-03 | 3.23 1.3e-03 | N/A | N/A | N/A | -3.71 2.2e-04 | N/A |
| Dentate nucleus left | 3.16 1.7e-03 | -1.70 0.09 | 3.62 3.1e-04 | N/A | N/A | N/A | -1.63 0.10 | -2.28 2.3e-02 |
| Pallidum right | 6.39 2.5e-10 | -5.12 3.8e-07 | -1.86 0.06 | N/A | N/A | N/A | -7.32 5.3e-13 | N/A |
| Pallidum left | 6.25 6.1e-10 | -4.92 1.0e-06 | -2.60 9.5e-03 | N/A | N/A | N/A | -7.80 1.7e-14 | N/A |
| Putamen right | 5.68 1.8e-08 | -4.61 4.5e-06 | -1.93 0.05 | N/A | N/A | N/A | -6.53 1.1e-10 | N/A |
| Putamen left | 5.18 2.8e-07 | -3.99 7.3e-05 | -3.52 4.5e-04 | N/A | N/A | N/A | -6.67 4.5e-11 | N/A |
| Red nucleus right | 5.52 4.3e-08 | -4.30 1.9e-05 | N/A | -2.95 3.2e-03 | 0.20 0.84 | -1.31 0.19 | -3.08 2.1e-03 | -1.50 0.13 |
| Red nucleus left | 4.62 4.4e-06 | -3.33 8.9e-04 | N/A | -2.43 1.5e-02 | 0.64 0.52 | -0.27 0.79 | -2.73 6.5e-03 | -1.62 0.11 |
| Substantia nigra right | 4.43 1.1e-05 | -3.17 1.6e-03 | N/A | -1.76 0.08 | 0.14 0.89 | -1.26 0.21 | -2.34 1.9e-02 | -1.48 0.14 |
| Substantia nigra left | 3.78 1.7e-04 | -2.52 1.2e-02 | N/A | N/A | N/A | N/A | -2.32 2.1e-02 | -2.03 4.3e-02 |

TABLE 4 Significance matrix showing the t-value (top number in a cell) p-value (bottom number in a cell) and direction for each variable and region for the eR₂* data. Note that the site and intercept variables are not shown and positive t-values indicate an increase with edwR₂ and a negative t-value indicates a decrease. N/A values are those which were removed by the AIC procedure

| Region | Age | Age squared | BMI percentile | Race | | | Sex male | Working memory speed z-score |
|------------------------|---------------|---------------|----------------|--------------|----------------|------------|---------------|------------------------------|
| | | | | Race black | Race caucasian | Race other | | |
| Dentate nucleus right | 7.54 1.1e-13 | N/A | -1.98 4.8e-02 | 2.13 3.3e-02 | 0.40 0.69 | 0.20 0.84 | -3.18 1.5e-03 | N/A |
| Dentate nucleus left | 9.73 2.3e-21 | N/A | -1.80 0.07 | N/A | N/A | N/A | -3.48 5.3e-04 | N/A |
| Pallidum right | 3.81 1.5e-04 | -2.83 4.8e-03 | -3.52 4.5e-04 | N/A | N/A | N/A | -5.68 1.8e-08 | -1.61 0.11 |
| Pallidum left | 3.74 2.0e-04 | -2.78 5.6e-03 | -3.52 4.6e-04 | N/A | N/A | N/A | -5.00 7.0e-07 | -1.98 4.8e-02 |
| Putamen right | 2.27 2.3e-02 | -1.69 0.09 | -4.96 8.2e-07 | N/A | N/A | N/A | -4.49 7.9e-06 | N/A |
| Putamen left | 8.84 4.8e-18 | N/A | -6.52 1.2e-10 | N/A | N/A | N/A | -4.49 8.0e-06 | N/A |
| Red nucleus right | 12.14 1.4e-31 | N/A | -5.15 3.2e-07 | -0.36 0.72 | 1.61 0.11 | -1.54 0.12 | N/A | -1.55 0.12 |
| Red nucleus left | 12.28 3.0e-32 | N/A | -4.66 3.6e-06 | -0.35 0.73 | 1.61 0.11 | -1.10 0.27 | N/A | -1.46 0.14 |
| Substantia nigra right | 3.39 7.3e-04 | -2.60 9.4e-03 | N/A | -1.88 0.06 | 0.01 0.99 | -1.68 0.09 | N/A | N/A |
| Substantia nigra left | 3.08 2.1e-03 | -2.28 2.3e-02 | -2.04 4.2e-02 | N/A | N/A | N/A | N/A | N/A |

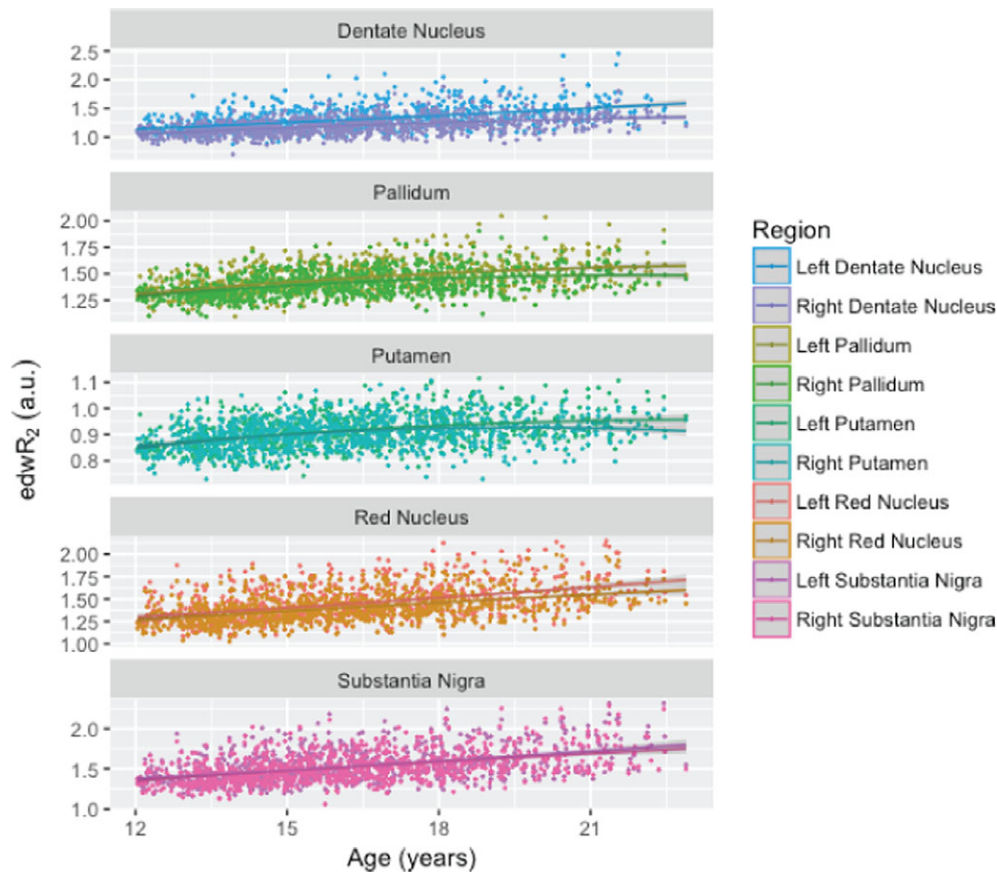


FIGURE 3 Normalized and covariate corrected baseline edwR₂ signal intensity plotted against age for the investigated regions on the left and right sides. All ROIs exhibited a significant age-related increase in edwR₂ [Color figure can be viewed at wileyonlinelibrary.com]

lower iron concentration in the bilateral pallidum, putamen, red nucleus, right dentate nucleus, and left substantia nigra. Faster working memory speed correlated with lower iron signal in the left pallidum. Relative to female participants, their male counterparts had lower iron signal in the bilateral dentate nucleus, pallidum, and putamen. These results are listed in Table 4 and the covariate-corrected age-signal plots are shown in Figure 4.

For the single site susceptibility data, the iron estimate was significantly greater with older age in all regions except left substantia nigra where age squared was a better fit. Lower BMI was related to greater iron content in the bilateral substantia nigra. African American subjects had significantly lower iron in the bilateral putamen and red nucleus, and right dentate nucleus and pallidum. Male subjects also had significantly higher iron content in the left substantia nigra than female participants. These results are listed in Table 5 and the covariate-corrected age-signal plots are shown in Figure 5.

3.4 | Relation of edwR₂ and eR₂* to QSM

The susceptibility data were significantly correlated with edwR₂ (Figure 6 and Table 6) and eR₂* (Figure 7 and Table 7). Across all regions, the *r*-squared for susceptibility relative to edwR₂ was 0.643 and for susceptibility relative to eR₂* was 0.578. The *r*-squared values for each region are shown in Table 8.

3.5 | Longitudinal edwR₂ and eR₂* analysis

For all three methods, the linear effects of age were highly significant. For eR₂* and QSM, only the linear age term was significant, but for edwR₂, there was a significant negative age-squared term for the red nucleus and putamen indicating decline in the rate of accumulation with advancing age. Table 9 presents the results for each method for each ROI and includes the slope and amount of variance explained by the fixed and the fix+random terms (Nakagawa & Schielzeth, 2013). Figures 8 and 9 present the longitudinal data for each bilateral ROI for edwR₂ and R₂*e.

Pearson correlations and intraclass correlations tested the correspondence of iron estimates between Times 1 and 2 and showed high reliability between sessions (Table 10 and Figure 10).

4 | DISCUSSION

A principal goal of this analysis was to investigate the success of repurposing DTI and fMRI data to estimate iron content in subcortical and cerebellar structures known to accrue iron over development. Strengths of the NCANDA data set include its sample sizes of well-characterized, healthy, male and female adolescents (Brown et al., 2015) and quality of the imaging data (Rohlfing et al., 2014). In light of evidence for continued neurodevelopment throughout adolescence and young adulthood (Stiles & Jernigan, 2010) and the need for

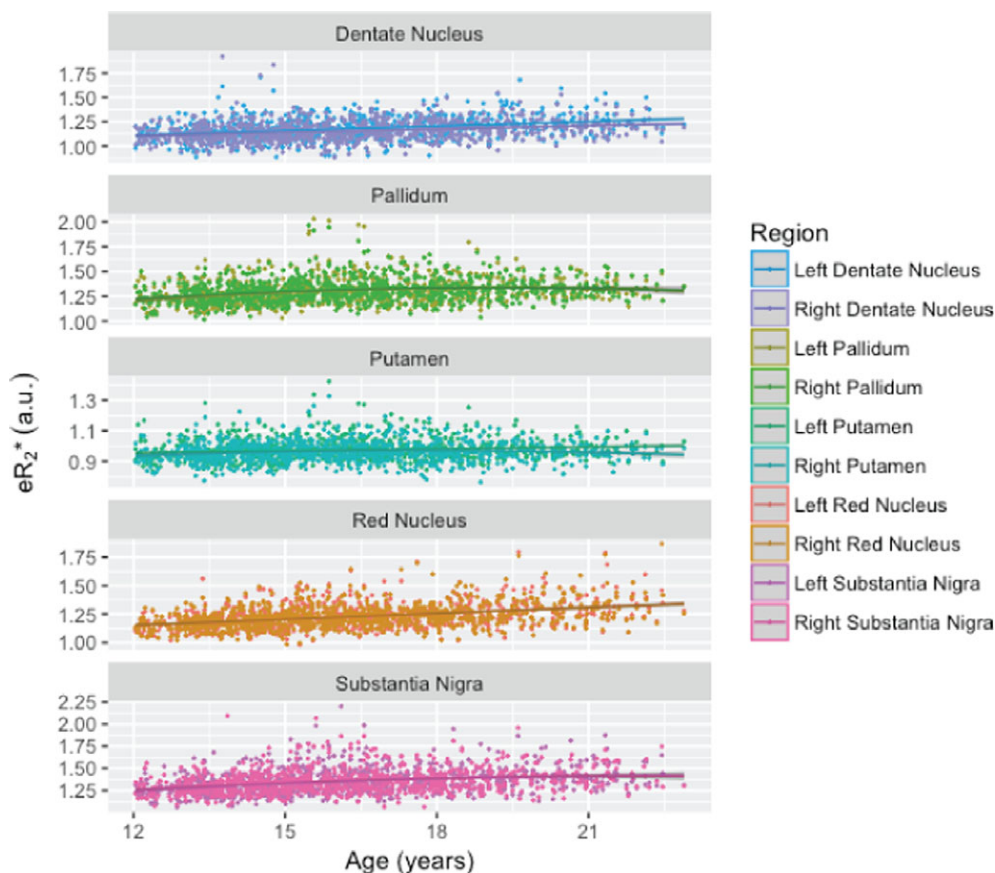


FIGURE 4 Normalized and covariate corrected baseline eR_2^* signal intensity plotted against age for the investigated regions on the left and right sides. All ROIs exhibited a significant age-related increase in estimated eR_2^* [Color figure can be viewed at [wileyonlinelibrary.com](#)]

nutrients including iron to support normal development of myelin, cognition, and dopamine function (Larsen & Luna, 2015), tracking the loci and accrual of nonheme iron can be a meaningful biomarker of gray matter development in adolescence in subcortical and cerebellar structures with MRI-detectable iron accumulation. The normalization procedure based on signal from the corpus callosum with its low iron content allowed for direct comparison of the images with each other without additional cross-site normalization. This procedure functioned robustly, in that no case was excluded due to improper normalization. The major counterindication to this normalization would be

any factor that disrupts the integrity or myelination of the corpus callosum, such as disease, damage, or image quality.

4.1 | Relations between iron metrics and demographic measures

The significant age-related decay rate for both eR_2^* and $edwR_2$ data in all ROIs indicates a linear, and often decelerating (age squared), relaxivity difference that corresponded well with known regional iron deposition amount, comporting with earlier reports

TABLE 5 Significance matrix showing the t -value (top number in a cell) p -value (bottom number in a cell) and direction for each variable and region for the susceptibility data. Note that the site and intercept variables are not shown and positive t -values indicate an increase with $edwR_2$ and a negative t -value indicates a decrease. N/A values are those which were removed by the AIC procedure. Unlike $edwR_2$ and eR_2^* , working memory speed was not significant for any region and was therefore omitted

| Region | Age | Age squared | BMI percentile | Race black | Race Caucasian | Race other | Sex male |
|------------------------|--------------|--------------|----------------|---------------|----------------|------------|--------------|
| Dentate nucleus right | 2.65 9.2e-03 | N/A | N/A | 2.00 4.8e-02 | 0.98 0.33 | 0.86 0.39 | N/A |
| Dentate nucleus left | 3.63 4.5e-04 | N/A | N/A | 1.97 0.05 | 0.98 0.33 | -0.07 0.95 | N/A |
| Pallidum right | 3.32 1.3e-03 | N/A | N/A | -2.35 2.1e-02 | -0.38 0.71 | 0.40 0.69 | N/A |
| Pallidum left | 4.00 1.2e-04 | N/A | N/A | -1.81 0.07 | -0.09 0.92 | -0.57 0.57 | N/A |
| Putamen right | 3.13 2.3e-03 | N/A | N/A | -3.24 1.6e-03 | -0.71 0.48 | 1.37 0.17 | -1.92 0.06 |
| Putamen left | 4.04 1.1e-04 | N/A | N/A | -3.11 2.4e-03 | -0.79 0.43 | 1.75 0.08 | N/A |
| Red nucleus right | 2.67 8.9e-03 | N/A | N/A | -2.77 6.6e-03 | -0.07 0.95 | 1.47 0.14 | N/A |
| Red nucleus left | 2.16 3.3e-02 | N/A | N/A | -2.10 3.8e-02 | 0.16 0.87 | 1.71 0.09 | N/A |
| Substantia nigra right | 3.82 2.4e-04 | N/A | -2.06 4.2e-02 | -0.37 0.71 | 0.76 0.45 | -1.06 0.29 | N/A |
| Substantia nigra left | N/A | 2.12 3.6e-02 | -2.49 1.4e-02 | N/A | N/A | N/A | 2.13 3.5e-02 |

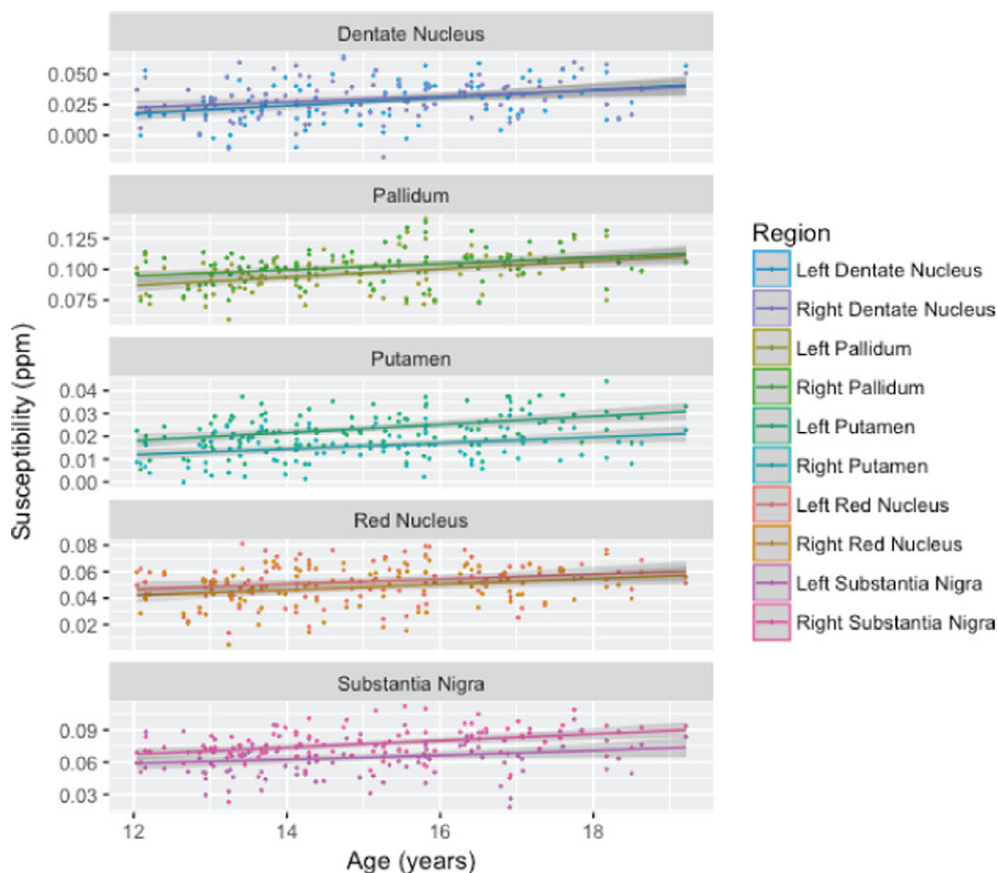


FIGURE 5 Susceptibility signal plotted against age for the investigated regions on the left and right sides. All ROIs exhibit a significant age-related increase in susceptibility, which is consistent with both $edwR_2$ and eR_2^* [Color figure can be viewed at wileyonlinelibrary.com]

(Daugherty & Raz, 2015; Daugherty & Raz, 2016; Hallgren & Sourander, 1958; Schenck & Zimmerman, 2004; Walsh & Han, 2014; Ward et al., 2014). Variables that were significant for the baseline analysis were BMI, working memory, and sex. Other

variables considered were supratentorial brain volume and handedness and did not have a significant relation with iron deposition measured in the brain. Greater iron deposition in specific brain regions identified in cross-sectional analysis corroborates previous results (Drayer et al., 1986; Hallgren & Sourander, 1958) but in a larger, younger sample of subjects rarely studied (Larsen & Luna, 2015). The effects of the age-squared term measured in vivo corroborate the deceleration of iron deposition previously reported in postmortem cases (Hallgren & Sourander, 1958).

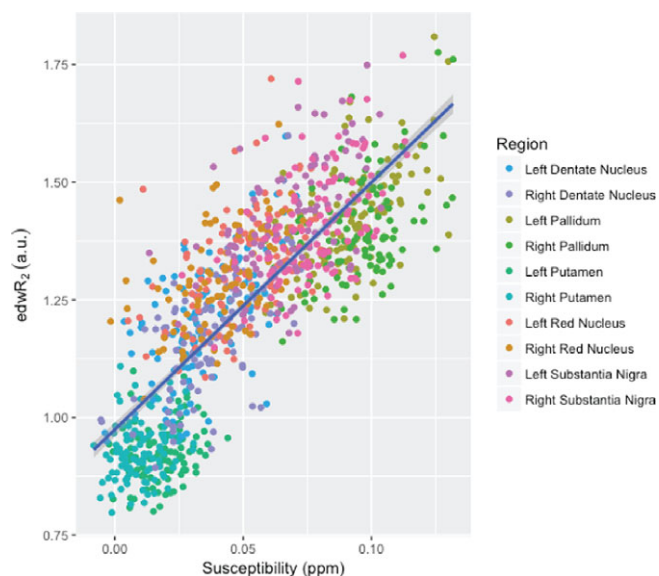


FIGURE 6 This figure compares the quantitative susceptibility with $edwR_2$. For all regions, an increasing susceptibility corresponds with an increased $edwR_2$ with an adjusted r -squared value of 0.643 [Color figure can be viewed at wileyonlinelibrary.com]

TABLE 6 Significance matrix showing the t -value and p -value for the intercept and average age for all regions for the longitudinal $edwR_2$ data. Positive t -values indicate an increase with $edwR_2$ and a negative t -value indicates a decrease

| Region | Intercept (t -, p -value) | Age (t -, p -value) |
|------------------------|--------------------------------|--------------------------|
| Dentate nucleus right | 1.24, 0.22 | -0.79, 0.43 |
| Dentate nucleus left | 0.09, 0.93 | 0.70, 0.49 |
| Pallidum right | 2.61, 9.4e-03 | -1.67, 0.10 |
| Pallidum left | 3.15, 1.7e-03 | -1.63, 0.10 |
| Putamen right | 1.44, 0.15 | -0.88, 0.38 |
| Putamen left | 2.26, 2.4e-02 | -0.71, 0.48 |
| Red nucleus right | 2.78, 5.8e-03 | -2.20, 2.8e-02 |
| Red nucleus left | 2.11, 3.5e-02 | -1.19, 0.23 |
| Substantia nigra right | 3.21, 1.4e-03 | -2.34, 2.0e-02 |
| Substantia nigra left | 1.82, 0.07 | -0.53, 0.60 |

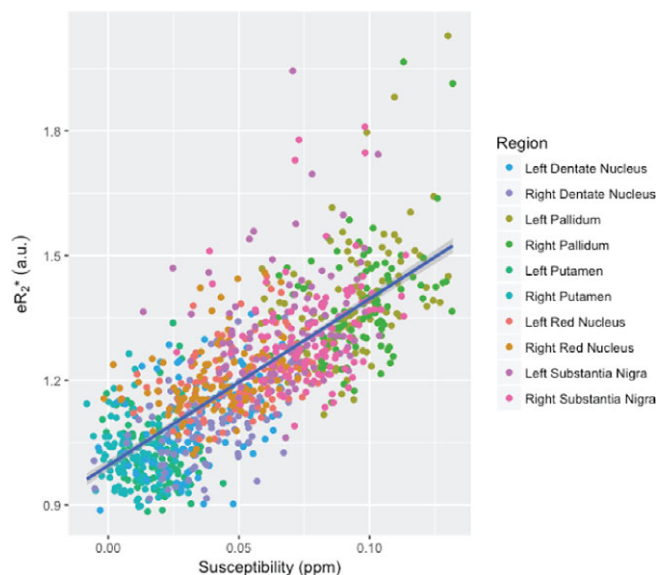


FIGURE 7 This figure compares the quantitative susceptibility with eR_2^* . For all regions, an increasing susceptibility corresponds with an increased eR_2^* with an adjusted r -squared value of 0.578 [Color figure can be viewed at wileyonlinelibrary.com]

While the age result was expected, the BMI and sex were not. BMI appears to be associated with both increasing and decreasing iron in the $edwR_2$ and eR_2^* . Sex differences, however, indicated significantly less iron in boys than girls across all ages and in almost all regions for both $edwR_2$ and eR_2^* data but not for QSM data, which were available for a smaller sample. While the observed sex difference was significant, it runs counter to some previous works (Bartzokis et al., 2007), although separate studies showed no gender difference. In addition, the other studies used older cohorts; thus, our study may subtend a stage of development where boys have less nonheme iron in the brain than girls (Xu, Wang, & Zhang, 2008), perhaps consistent with later maturation of boys than girls.

4.2 | Longitudinal $edwR_2$ and eR_2^* analysis

With a data set of 385 subjects and approximately a year separating the scans, we were able to detect significant age effects, both in the

TABLE 7 Significance matrix showing the t -value and p -value for the intercept and average age for all regions for the longitudinal eR_2^* data. Positive t -values indicate an increase with $edwR_2$ and a negative t -value indicates a decrease

| Region | Intercept (t -, p -value) | Age (t -, p -value) |
|------------------------|--------------------------------|--------------------------|
| Dentate nucleus right | 1.54, 0.13 | -1.09, 0.27 |
| Dentate nucleus left | 0.95, 0.34 | -0.52, 0.60 |
| Pallidum right | -0.03, 0.98 | 0.66, 0.51 |
| Pallidum left | -0.50, 0.61 | 1.43, 0.15 |
| Putamen right | -1.10, 0.27 | 1.32, 0.19 |
| Putamen left | -0.35, 0.73 | 0.97, 0.33 |
| Red nucleus right | 2.17, 3.1e-02 | -1.78, 0.08 |
| Red nucleus left | 2.10, 3.6e-02 | -1.60, 0.11 |
| Substantia nigra right | 0.46, 0.65 | -0.16, 0.88 |
| Substantia nigra left | 1.10, 0.27 | -0.66, 0.51 |

TABLE 8 r -squared values for $edwR_2$ and eR_2^* for all regions when compared to susceptibility. All $edwR_2$ r -squared values are higher than their eR_2^* counterparts

| Region | $edwR_2$ | eR_2^* |
|------------------------|----------|----------|
| Dentate nucleus left | 0.369 | 0.149 |
| Dentate nucleus right | 0.381 | 0.166 |
| Pallidum left | 0.317 | 0.188 |
| Pallidum right | 0.211 | 0.133 |
| Putamen left | 0.041 | -0.003 |
| Putamen right | 0.047 | 0.018 |
| Red nucleus left | 0.236 | 0.115 |
| Red nucleus right | 0.208 | 0.096 |
| Substantia nigra left | 0.264 | 0.035 |
| Substantia nigra right | 0.248 | 0.046 |

intercept and slope—similar to age and age squared in the full analysis. This longitudinal analysis corroborates the trend of greater iron presence with older age measured in the baseline cross-sectional data using nonquantitative scans.

4.3 | Relation of $edwR_2$ and eR_2^* to QSM

The QSM results from the susceptibility scan showed that the susceptibility was greater with older age as a group and visit for individual subjects. These results indicated presence of iron deposition in all regions, thereby corroborating the $edwR_2$ and eR_2^* from the DTI and fMRI scans. Thus, despite the nonquantitative nature of raw signal in DTI and fMRI scans as reflecting iron presence, quantitative information could be inferred from them. Recently, iron was detected using T1 hyperintensity signal in the pallidum of patients with liver cirrhosis (Lee et al., 2018). Although comparison with QSM revealed good agreement, use of the T1 hyperintensity signal may require pathology that causes the hyperintensity, thereby making the iron signal visible but perhaps inadequate for detection of normal developmental effects. In addition, the susceptibility increase seen in the QSM data indicates that the change is occurring through iron deposition or demyelination while the increasing $edwR_2^*$ and eR_2^* indicate increasing iron and/or myelin content. Because both QSM and R_2^* measures are increasing this leads to the likely conclusion that the process is that of iron deposition rather than significant changes in myelin (Duyn & Schenck, 2017; Liu, Li, et al., 2015).

4.4 | fMRI data for iron quantification: $edwR_2$ versus eR_2^*

Despite use of fMRI data to quantify regional iron deposition, the r -squared values for all regions for $edwR_2$ were higher than eR_2^* when compared with susceptibility from QSM (Table 4) (Haacke et al., 2005; Li et al., 2011; Li et al., 2014; Liu, Li, et al., 2015). This initially counterintuitive result is likely attributable to ferritin, which shortens the T_1 (Haacke et al., 2005) and increases the fMRI signal contrary to the decreased signal from a shortened T_2^* . This antagonistic signal effect is not present in DTI data because the TR is 8 s for DTI, which allows near complete recovery compared to the 2.2 s recovery time used for fMRI data.

TABLE 9 Results of linear mixed-effects models

| | linear_age_t | linear_age_p | age_slope_%/year | linear_fixed | linear_fixed+random | Best fit | | | |
|--------------------|--------------|--------------|------------------|--------------|---------------------|------------------------|------------|-------------------|-----------|
| edwR2 | | | | | | | | | |
| Dentate_Nucleus | 11.3849 | 0.0000 | 2.2104 | 0.1554 | 0.9087 | Linear | | | |
| Red_Nucleus | 13.9364 | 0.0000 | 1.6804 | 0.2083 | 0.9232 | Quadratic [†] | | | |
| Putamen | 10.9435 | 0.0000 | 1.0837 | 0.1643 | 0.8636 | Quadratic [†] | | | |
| Pallidum | 11.4545 | 0.0000 | 1.9845 | 0.1557 | 0.9109 | Linear | | | |
| Substantia_Nigra | 13.5681 | 0.0000 | 2.3529 | 0.2074 | 0.9141 | Linear | | | |
| eR2* | | | | | | | | | |
| Dentate_Nucleus | 7.6555 | 0.0000 | 1.1690 | 0.0974 | 0.7139 | Linear | | | |
| Red_Nucleus | 6.7634 | 0.0000 | 0.9126 | 0.0561 | 0.9162 | Linear | | | |
| Putamen | 3.081 | 0.0021 | 0.3421 | 0.0144 | 0.8690 | Linear | | | |
| Pallidum | 9.915 | 0.0000 | 1.3823 | 0.1532 | 0.6771 | Linear | | | |
| Substantia_Nigra | 7.2956 | 0.0000 | 1.1584 | 0.0885 | 0.7392 | Linear | | | |
| Susceptibility | | | | | | | | | |
| Dentate_Nucleus | 5.0861 | 0.0000 | 8.4660 | 0.1655 | 0.8069 | Linear | | | |
| Red_Nucleus | 3.2359 | 0.0015 | 2.0320 | 0.0640 | 0.8577 | Linear | | | |
| Putamen | 2.9878 | 0.0034 | 8.4665 | 0.0706 | 0.6426 | Linear | | | |
| Pallidum | 4.65 | 0.0000 | 7.1322 | 0.1305 | 0.8477 | Linear | | | |
| Substantia_Nigra | 6.7832 | 0.0000 | 5.6470 | 0.2807 | 0.7309 | Linear | | | |
| edwR2 [†] | | | | | | | | | |
| ROI | quad_age_t | quad_age_p | age_slope_%/year | quad_age_2_t | quad_age_2_p | Age_2_slope_%/year | quad_fixed | quad_fixed+random | best_fit |
| Red_Nucleus | 4.4916 | 0.0000 | 4.8432 | -2.9516 | 0.0033 | -0.0946 | 0.2057 | 0.9229 | Quadratic |
| Putamen | 3.7100 | 0.0002 | 3.5793 | -2.6018 | 0.0095 | -0.0744 | 0.1647 | 0.8622 | Quadratic |

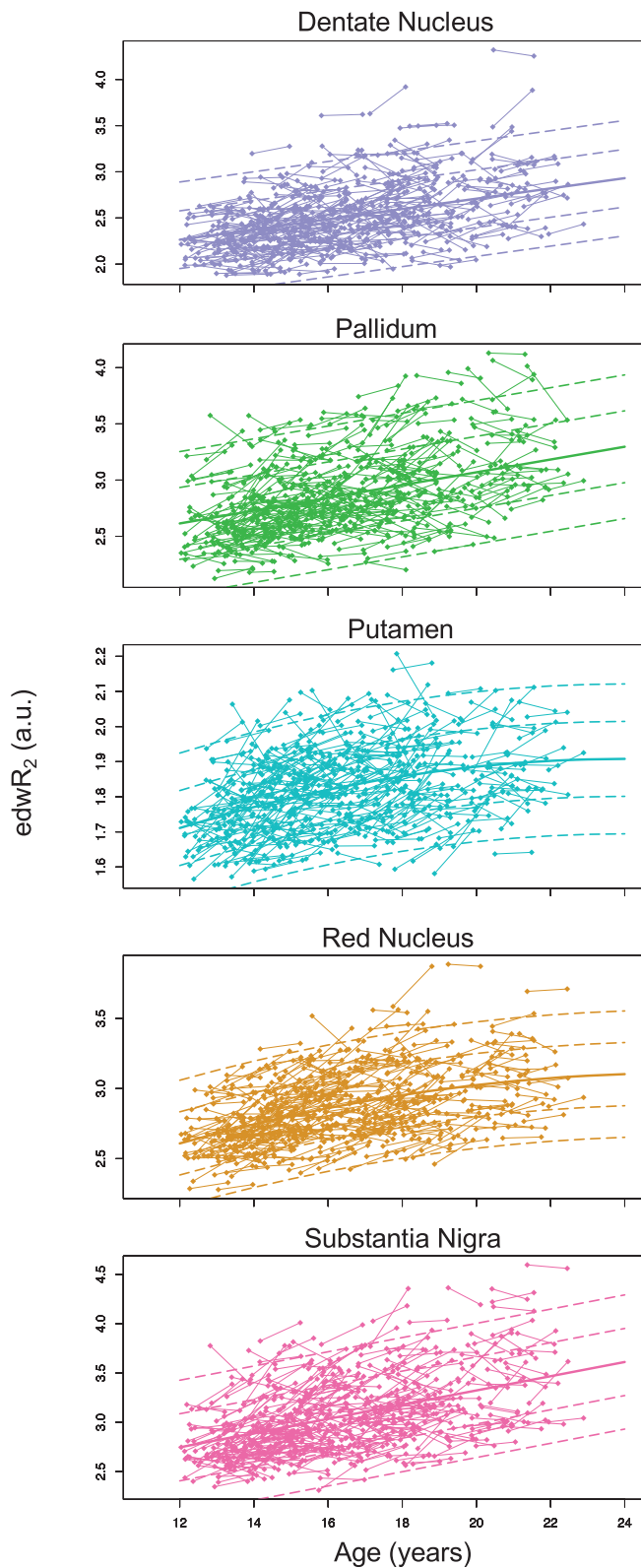


FIGURE 8 Results of lme analysis of longitudinal $edwR_2$ fits. Solid lines are predicted scores at each age, dashed lines are ± 1 and $2 SD$ [Color figure can be viewed at wileyonlinelibrary.com]

4.5 | DTI data for iron quantification: $edwR_2$ versus eR_2^*

The differences between eR_2^* (i.e., without diffusion gradients on) and $edwR_2$ (i.e., with diffusion gradients on) are due to the near

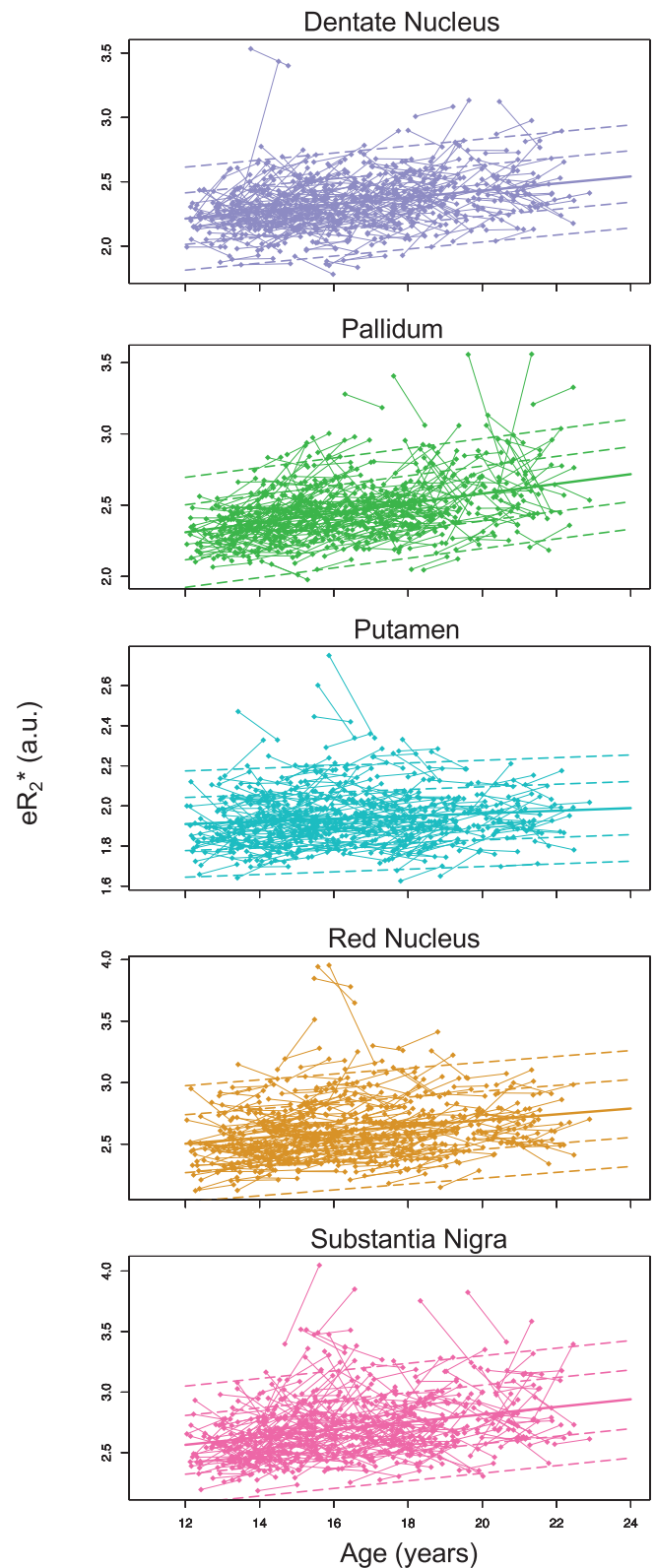


FIGURE 9 Results of lme analysis of longitudinal eR_2^* fits. Solid lines are predicted scores at each age; dashed lines are ± 1 and $2 SD$ [Color figure can be viewed at wileyonlinelibrary.com]

complete reduction of diffusing and flowing signal. Most obviously, this causes the CSF signal to be nearly extinguished, but it also reduces the signal from all diffusing materials in the brain. The reason for the better performance of the $edwR_2$ may be due to extraneous

TABLE 10 Time 1-time 2 correlations

| | ICC | r | t | p | df |
|-------------------|-------|-------|--------|----------|-----|
| edwR ₂ | | | | | |
| Dentate_Nucleus | 0.911 | 0.916 | 44.659 | <2.2e-16 | 383 |
| Red_Nucleus | 0.901 | 0.920 | 46.036 | <2.2e-16 | 383 |
| Putamen | 0.831 | 0.856 | 32.449 | <2.2e-16 | 383 |
| Pallidum | 0.910 | 0.917 | 44.898 | <2.2e-16 | 383 |
| Substantia_Nigra | 0.900 | 0.916 | 44.548 | <2.2e-16 | 383 |
| eR ₂ * | | | | | |
| Dentate_Nucleus | 0.706 | 0.714 | 19.934 | <2.2e-16 | 382 |
| Red_Nucleus | 0.909 | 0.916 | 44.706 | <2.2e-16 | 383 |
| Putamen | 0.866 | 0.873 | 35.078 | <2.2e-16 | 383 |
| Pallidum | 0.671 | 0.678 | 18.037 | <2.2e-16 | 383 |
| Substantia_Nigra | 0.737 | 0.741 | 21.595 | <2.2e-16 | 383 |
| QSM | | | | | |
| Dentate_Nucleus | 0.763 | 0.801 | 10.946 | <2.2e-16 | 67 |
| Red_Nucleus | 0.849 | 0.866 | 14.195 | <2.2e-16 | 67 |
| Putamen | 0.620 | 0.629 | 6.617 | 7.31E-09 | 67 |
| Pallidum | 0.772 | 0.840 | 12.662 | <2.2e-16 | 67 |
| Substantia_Nigra | 0.655 | 0.719 | 8.476 | 3.35E-12 | 67 |

signal suppression; alternatively, the cause may also be simple SNR difference because of the number of images entered into the averages: 60 diffusion-weighted volumes for edwR₂ versus two nondiffusion-weighted volumes for eR₂*

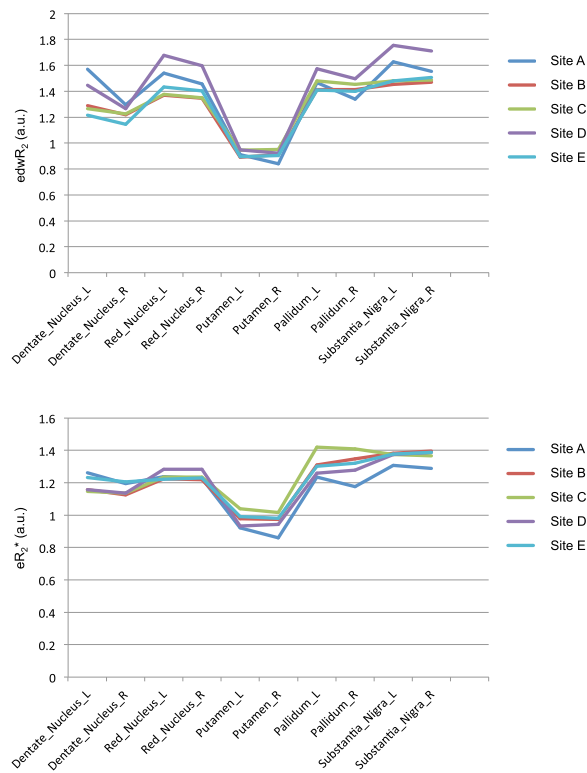


FIGURE 10 Profiles of DTI edwR₂ (top) and fMRI eR₂* (bottom) iron estimates for the five ROIs by the five collection sites. The figures show that the two profiles by sites are highly similar as supported by the lack of interactions involving site [Color figure can be viewed at wileyonlinelibrary.com]

4.6 | Limitations

The collection site effects remained highly significant despite the individual subject intensity normalization and the inclusion of demographic variables such as BMI. The substitution of a scanner manufacturer variable for site was also significant, but with the manufacturer variable there remained significant site differences and was, therefore, removed in favor of the more flexible site variable. This difference suggests that the site differences are primarily systematic system, positioning, coil, or physical differences between the sites.

The nonquantitative nature of this approach requires a site variable to remove the remaining site differences, but through that addition, this method remains compatible with multiple sites, and GE and Siemens systems. In addition, a site correction such as removing the mean difference between the sites or matching the histograms could take the place of the site variable, but this was not explored in this work. Ideally though, longitudinal analysis would be performed which removes the need for site normalization. Any of these approaches allows for post hoc analysis of multicenter data that would otherwise not be available for analysis.

A major limitation of the reference approach is attributable to the colocalization of iron and myelin in the brain, making it difficult to distinguish the effects of the two on the measured signal. One approach for differentiating the contribution of myelin from iron is to collect both QSM and R₂* data. Because myelin is diamagnetic and iron is paramagnetic, both iron and myelin increase the R₂* value, but in QSM, greater myelin presence decreases susceptibility while greater iron presence increases susceptibility. In the subset of subjects for whom we have both modalities, we detected greater R₂* and greater QSM values, providing evidence for the conclusion that the majority of the change is driven by iron deposition. This convergence lends support to the extrapolation that the results of all subjects in this study follow the same pattern.

5 | CONCLUSIONS

This work demonstrates that DTI and fMRI data, while unable to measure iron concentration quantitatively, can be repurposed as an analog of brain iron deposition. This conclusion was directly verified with QSM imaging, which is the current standard for noninvasive in vivo quantification of nonheme iron. Further support for this conclusion stemmed from our preliminary longitudinal results from the same set of subjects. The analysis outlined herein allows the estimation of iron with the use of commonly used DTI and fMRI acquisitions rather than the less frequently used SWI acquisitions. It also allows post hoc iron analysis of data sets acquired even before SWI acquisition and QSM approaches were developed.

Tracking normal iron deposition trajectories could enable detection of developmental deviations marking accelerated brain tissue shrinkage (Daugherty & Raz, 2016), apoptosis (Ward et al., 2014), and demyelination (Bartzokis, 2011; Bartzokis et al., 2011) associated with oxidative stress and abnormal dopamine and serotonin metabolism (Larsen & Luna, 2015; Otero, Pliego-Rivero, Porcayo-Mercado, & Mendieta-Alcántara, 2008) potentially resulting from chronic,

excessive alcohol use (Bühler & Mann, 2011; Wang, Shum, Lin, & Wang, 1996). Indeed, the relation between low iron estimates and greater BMI and lower working memory scores may reflect poor nutritional developmental or current status (cf., Beard & Connor, 2003). It could also be used to monitor aging trajectories and diseases such as further studies of Alzheimer's, Parkinson's, multiple sclerosis, anemia, HIV/AIDS, among others.

ACKNOWLEDGMENTS

This work was supported by the National Institutes of Health: AA021697, AA021695, AA021692, AA021696, AA021681, AA021690, AA021691, K05 AA017168, and the Moldow Women's Hope and Healing Fund.

CONFLICT OF INTERESTS

The authors declare no competing conflict of interests.

ORCID

Edith V. Sullivan  <https://orcid.org/0000-0001-6739-3716>

REFERENCES

- Andersson, J. L. R., & Skare, S. (2002). A model-based method for retrospective correction of geometric distortions in diffusion-weighted EPI. *NeuroImage*, *16*, 177–199.
- Avants, B. B., Epstein, C. L., Grossman, M., & Gee, J. C. (2008). Symmetric diffeomorphic image registration with cross-correlation: Evaluating automated labeling of elderly and neurodegenerative brain. *Medical Image Analysis*, *12*, 26–41.
- Bartzokis, G. (2011). Alzheimer's disease as homeostatic responses to age-related myelin breakdown. *Neurobiology of Aging*, *32*, 1341–1371.
- Bartzokis, G., Lu, P. H., Tingus, K., Peters, D. G., Amar, C. P., Tishler, T. A., ... Connor, J. R. (2011). Gender and iron genes may modify associations between brain iron and memory in healthy aging. *Neuropsychopharmacology*, *36*, 1375–1384.
- Bartzokis, G., Mintz, J., Sultzer, D., Marx, P., Herzberg, J. S., Phelan, C. K., & Marder, S. R. (1994). In vivo MR evaluation of age-related increases in brain iron. *American Journal of Neuroradiology*, *15*, 1129–1138.
- Bartzokis, G., Tishler, T. A., Lu, P. H., Villablanca, P., Altschuler, L. L., Carter, M., ... Mintz, J. (2007). Brain ferritin iron may influence age- and gender-related risks of neurodegeneration. *Neurobiology of Aging*, *28*, 414–423.
- Beard, J. L., & Connor, J. R. (2003). Iron status and neural functioning. *Annual Review of Nutrition*, *23*, 41–58.
- Blasco, G., Puig, J., Daunis-I-Estadella, J., Molina, X., Xifra, G., Fernández-Aranda, F., ... Fernández-Real, J. M. (2014). Brain iron overload, insulin resistance, and cognitive performance in obese subjects: A preliminary MRI case-control study. *Diabetes Care*, *37*, 3076–3083.
- Brown, S. A., Brumback, T., Tomlinson, K., Cummins, K., Thompson, W. K., Nagel, B. J., ... Tapert, S. F. (2015). The National Consortium on Alcohol and NeuroDevelopment in Adolescence (NCANDA): A multisite study of adolescent development and substance use. *Journal of Studies on Alcohol and Drugs*, *76*, 895–908.
- Bühler, M., & Mann, K. (2011). Alcohol and the human brain: A systematic review of different neuroimaging methods. *Alcoholism: Clinical and Experimental Research*, *35*, 1771–1793.
- Casey, B. J., Jones, R. M., & Hare, T. A. (2008). The adolescent brain. *Annals of the New York Academy of Sciences*, *1124*, 111–126.
- Daugherty, A. M., & Raz, N. (2015). Appraising the role of iron in brain aging and cognition: Promises and limitations of MRI methods. *Neuropsychology Review*, *25*, 272–287.
- Daugherty, A. M., & Raz, N. (2016). Accumulation of iron in the putamen predicts its shrinkage in healthy older adults: A multi-occasion longitudinal study. *NeuroImage*, *128*, 11–20.
- Deoni, S., Dean, D., III, Joelson, S., O'Regan, J., & Schneider, N. (2018). Early nutrition influences developmental myelination and cognition in infants and young children. *NeuroImage*, *178*, 649–659.
- Dhenain, M., Michot, J. L., Volk, A., Picq, J. L., & Boller, F. (1997). T2-weighted MRI studies of mouse lemurs: A primate model of brain aging. *Neurobiology of Aging*, *18*, 517–521.
- Diedrichsen, J. (2006). A spatially unbiased atlas template of the human cerebellum. *NeuroImage*, *33*, 127–138.
- Drayer, B., Burger, P., Darwin, R., Riederer, S., Herfkens, R., & Johnson, G. A. (1986). MRI of brain iron. *American Journal of Roentgenology*, *147*, 103–110.
- Duyn, J. H., & Schenck, J. (2017). Contributions to magnetic susceptibility of brain tissue. *NMR in Biomedicine*, *30*, e3546.
- Fukunaga, M., Li, T. Q., van Gelderen, P., de Zwart, J. A., Shmueli, K., Yao, B., ... Duyn, J. H. (2010). Layer-specific variation of iron content in cerebral cortex as a source of MRI contrast. *Proceedings of the National Academy of Sciences of the United States of America*, *107*, 3834–3839.
- Gelman, N., Gorell, J. M., Barker, P. B., Savage, R. M., Spickler, E. M., Windham, J. P., & Knight, R. A. (1999). MR imaging of human brain at 3.0 T: Preliminary report on transverse relaxation rates and relation to estimated iron content. *Radiology*, *210*, 759–767.
- Glasser, M. F., Coalson, T. S., Robinson, E. C., Hacker, C. D., Harwell, J., Yacoub, E., ... Van Essen, D. C. (2016). A multi-modal parcellation of human cerebral cortex. *Nature*, *536*, 1–11.
- Glasser, M. F., & Van Essen, D. C. (2011). Mapping human cortical areas in vivo based on myelin content as revealed by T1- and T2-weighted MRI. *The Journal of Neuroscience: The Official Journal of the Society for Neuroscience*, *31*, 11597–11616.
- Gur, R. C., Richar, J., Hughett, P., Calkins, M. E., Macy, L., Bilker, W. B., ... Gur, R. E. (2010). A cognitive neuroscience based computerized battery for efficient measurement of individual differences: Standardization and initial construct validation. *Journal of Neuroscience Methods*, *187*, 254–262.
- Haacke, E. M., Cheng, N. Y. C., House, M. J., Liu, Q., Neelavalli, J., Ogg, R. J., ... Obenaus, A. (2005). Imaging iron stores in the brain using magnetic resonance imaging. *Magnetic Resonance Imaging*, *23*, 1–25.
- Hallgren, B., & Sourander, P. (1958). The effect of age on the non-haemin iron in the human brain. *Journal of Neurochemistry*, *3*, 41–51.
- Hallgren, B., & Sourander, P. (1960). The non-haemin iron in the cerebral cortex in Alzheimer's disease. *Journal of Neurochemistry*, *5*, 307–310.
- Jenkinson, M., & Smith, S. (2001). A global optimisation method for robust affine registration of brain images. *Medical Image Analysis*, *5*, 143–156.
- Kullmann, S., Callaghan, M. F., Heni, M., Weiskopf, N., Scheffler, K., Häring, H. U., ... Preissl, H. (2016). Specific white matter tissue microstructure changes associated with obesity. *NeuroImage*, *125*, 36–44.
- Langkammer, C., Krebs, N., Goessler, W., Scheurer, E., Ebner, F., Yen, K., ... Ropele, S. (2010). Quantitative MR imaging of brain iron: A postmortem validation study. *Radiology*, *257*, 455–462.
- Larsen, B., & Luna, B. (2015). In vivo evidence of neurophysiological maturation of the human adolescent striatum. *Developmental Cognitive Neuroscience*, *12*, 74–85.
- Lebel, C., Walker, L., Leemans, A., Phillips, L., & Beaulieu, C. (2008). Microstructural maturation of the human brain from childhood to adulthood. *NeuroImage*, *40*, 1044–1055.
- Lee, S., Nam, Y., Jang, J., Na, G. H., Kim, D. G., Shin, N. Y., ... Kim, B. S. (2018). Deep gray matter iron measurement in patients with liver cirrhosis using quantitative susceptibility mapping: Relationship with pallidal T1 hyperintensity. *Journal of Magnetic Resonance Imaging*, *47*, 1342–1349.
- Li, W., Wu, B., Batrachenko, A., Bancroft-Wu, V., Morey, R. A., Shashi, V., ... Liu, C. (2014). Differential developmental trajectories of magnetic susceptibility in human brain gray and white matter over the lifespan. *Human Brain Mapping*, *35*, 2698–2713.
- Li, W., Wu, B., & Liu, C. (2011). Quantitative susceptibility mapping of human brain reflects spatial variation in tissue composition. *NeuroImage*, *55*, 1645–1656.

- Liu, C., Li, W., Tong, K. A., Yeom, K. W., & Kuzminski, S. (2015). Susceptibility-weighted imaging and quantitative susceptibility mapping in the brain. *Journal of Magnetic Resonance Imaging*, 42, 23–41.
- Liu, J., Lee, H. J., Weitz, A. J., Fang, Z., Lin, P., Choy, M., ... Lee, J. H. (2015). Frequency-selective control of cortical and subcortical networks by central thalamus. *eLife*, 4, 1–27.
- Müller-Oehring, E. M., Kwon, D., Nagel, B. J., Sullivan, E. V., Chu, W., Rohlfing, T., ... Pohl, K. M. (2018). Influences of age, sex, and moderate alcohol drinking on the intrinsic functional architecture of adolescent brains. *Cerebral Cortex*, 28(3), 1049–1063.
- Nakagawa, S., & Schielzeth, H. (2013). A general and simple method for obtaining R^2 from generalized linear mixed-effects models. *Methods in Ecology and Evolution*, 4, 133–142.
- Nichols, B. N. (2015). Neuroinformatics software applications supporting electronic data capture, management, and sharing for the neuroimaging community. *Neuropsychology Review*, 25, 356–368.
- Otero, G. A., Pliego-Rivero, F. B., Porcayo-Mercado, R., & Mendieta-Alcántara, G. (2008). Working memory impairment and recovery in iron deficient children. *Clinical Neurophysiology*, 119, 1739–1746.
- Pfefferbaum, A., Adalsteinsson, E., Rohlfing, T., & Sullivan, E. V. (2009). MRI estimates of brain iron concentration in normal aging: Comparison of field-dependent (FDRI) and phase (SWI) methods. *NeuroImage*, 47, 493–500.
- Pfefferbaum, A., Adalsteinsson, E., Rohlfing, T., & Sullivan, E. V. (2010). Diffusion tensor imaging of deep gray matter brain structures: Effects of age and iron concentration. *Neurobiology of Aging*, 31, 482–493.
- Pfefferbaum, A., Kwon, D., Brumback, T., Thompson, W. K., Cummins, K., Tapert, S. F., ... Sullivan, E. V. (2018). Altered brain developmental trajectories in adolescents after initiating drinking. *The American Journal of Psychiatry*, 175, 370–380.
- Pfefferbaum, A., Rohlfing, T., Pohl, K. M., Lane, B., Chu, W., Kwon, D., ... Sullivan, E. V. (2016). Adolescent development of cortical and white matter structure in the NCANDA sample: Role of sex, ethnicity, puberty, and alcohol drinking. *Cerebral Cortex*, 26, 4101–4121.
- Pohl, K. M., Sullivan, E. V., Rohlfing, T., Chu, W., Kwon, D., Nichols, B. N., ... Pfefferbaum, A. (2016). Harmonizing DTI measurements across scanners to examine the development of white matter microstructure in 803 adolescents of the NCANDA study. *NeuroImage*, 130, 194–213.
- Poynton, C. B., Jenkinson, M., Adalsteinsson, E., Sullivan, E. V., Pfefferbaum, A., & Wells, W. (2015). Quantitative susceptibility mapping by inversion of a perturbation field model: Correlation with brain iron in normal aging. *IEEE Transactions on Medical Imaging*, 34, 339–353.
- Rodríguez, K. M., Haacke, E. M., & Raz, N. (2011). Differential effects of age and history of hypertension on regional brain volumes and iron. *NeuroImage*, 54, 750–759.
- Rohlfing, T., Cummins, K., Henthorn, T., Chu, W., & Nichols, B. N. (2014). N-CANDA data integration: Anatomy of an asynchronous infrastructure for multi-site, multi-instrument longitudinal data capture. *Journal of the American Medical Informatics Association*, 21, 758–762.
- Rohlfing, T., Zahr, N. M., Sullivan, E. V., & Pfefferbaum, A. (2010). The SRI24 multichannel atlas of normal adult human brain structure. *Human Brain Mapping*, 31, 798–819.
- Ropele, S., & Langkammer, C. (2016). Iron quantification with susceptibility. *NMR in Biomedicine*, 77(4), 1562–1572.
- Schenck, J. F., & Zimmerman, E. A. (2004). High-field magnetic resonance imaging of brain iron: Birth of a biomarker? *NMR in Biomedicine*, 17, 433–445.
- Smith, S. M., Jenkinson, M., Woolrich, M. W., Beckmann, C. F., Behrens, T. E. J., Johansen-Berg, H., ... Matthews, P. M. (2004). Advances in functional and structural MR image analysis and implementation as FSL. *NeuroImage*, 23(Suppl. 1), S208–S219.
- Stiles, J., & Jernigan, T. L. (2010). The basics of brain development. *Neuropsychology Review*, 20, 327–348.
- Sullivan, E. V., Brumback, T., Tapert, S. F., Fama, R., Prouty, D., Brown, S. A., ... Pfefferbaum, A. (2016). Cognitive, emotion control, and motor performance of adolescents in the NCANDA study: Contributions from alcohol consumption, age, sex, ethnicity, and family history of addiction. *Neuropsychology*, 30, 449–473.
- Van Rossum, G. (1991). *Python 2.7*. Python Software Foundation. Stichting Mathematisch Centrum Amsterdam, The Netherlands.
- Venables, W. N., & Ripley, B. D. (2002). *Modern applied statistics with S*. Statistics and computing. Springer, NY.
- Vymazal, J., Brooks, R. A., Patronas, N., Hajek, M., Bulte, J. W., & Di Chiro, G. (1995). Magnetic resonance imaging of brain iron in health and disease. *Journal of the Neurological Sciences*, 134(Suppl), 19–26.
- Vymazal, J., Righini, A., Brooks, R. A., Canesi, M., Mariani, C., Leonardi, M., & Pezzoli, G. (1999). T1 and T2 in the brain of healthy subjects, patients with Parkinson disease, and patients with multiple system atrophy: Relation to iron content. *Radiology*, 211, 489–495.
- Walsh, J. J., & Han, M. H. (2014). The heterogeneity of ventral tegmental area neurons: Projection functions in a mood-related context. *Neuroscience*, 282, 101–108.
- Wang, J. Y., Shum, A. Y. C., Lin, T. C., & Wang, Y. (1996). Central serotonergic lesions increase voluntary alcohol consumption in Sprague Dawley rats: Moderation by long-term ethanol administration. *Alcoholism: Clinical and Experimental Research*, 20, 1252–1259.
- Ward, R. J., Zucca, F. A., Duyn, J. H., Crichton, R. R., & Zecca, L. (2014). The role of iron in brain ageing and neurodegenerative disorders. *The Lancet Neurology*, 13, 1045–1060.
- Xu, X., Wang, Q., & Zhang, M. (2008). Age, gender, and hemispheric differences in iron deposition in the human brain: An in vivo MRI study. *NeuroImage*, 40, 35–42.
- Zhang, Y., Wei, H., Cronin, M. J., He, N., Yan, F., & Liu, C. (2018). Longitudinal atlas for normative human brain development and aging over the lifespan using quantitative susceptibility mapping. *NeuroImage*, 171, 176–189.

How to cite this article: Peterson ET, Kwon D, Luna B, et al. Distribution of brain iron accrual in adolescence: Evidence from cross-sectional and longitudinal analysis. *Hum Brain Mapp*. 2019;40:1480–1495. <https://doi.org/10.1002/hbm.24461>